



PAPER

Self-powering vibration sensor based on a cantilever system with a single-electrode mode triboelectric nanogenerator

To cite this article: Sagar Hosangadi Prutvi *et al* 2022 *Meas. Sci. Technol.* **33** 075115

View the [article online](#) for updates and enhancements.

You may also like

- [Ionic hydrogels-based triboelectric nanogenerators for self-powered human-machine interfaces](#)
Siyang Liang, Chang Li, Mengjuan Niu et al.
- [Nanogenerator for scavenging low frequency vibrations](#)
Jae Yeong Park, Md Salauddin and M Salauddin Rasel
- [From contact electrification to triboelectric nanogenerators](#)
Zhong Lin Wang

PRIME
PACIFIC RIM MEETING
ON ELECTROCHEMICAL
AND SOLID STATE SCIENCE

HONOLULU, HI
Oct 6–11, 2024

Abstract submission deadline:
April 12, 2024

Learn more and submit!

Joint Meeting of

The Electrochemical Society

•

The Electrochemical Society of Japan

•

Korea Electrochemical Society

A woman in a black jacket and yellow lanyard stands in front of a poster board. A man in a blue shirt and glasses points at a poster. Another person is visible in the background.

Self-powering vibration sensor based on a cantilever system with a single-electrode mode triboelectric nanogenerator

Sagar Hosangadi Prutvi, Mallikarjuna Korrapati and Dipti Gupta*

Metallurgical Engineering and Materials Science Department, Indian Institute of Technology Bombay, Powai, 400076, India

E-mail: diptig@iitb.ac.in

Received 26 November 2021, revised 18 February 2022

Accepted for publication 7 March 2022

Published 28 April 2022



Abstract

Here, we report a vibration sensor based on a single-electrode mode triboelectric nanogenerator (TENG). The main objective of this study is to develop a vibration sensor (architecture) that can be employed in any application with minor design changes to meet individual objectives. Hence, a cantilever-based vibration system is selected, which offers optimum design control in fine-tuning the sensor to operate in the desired frequency spectrum. The cantilever's proof mass is suspended by isotropic linear elastic material constituting a scalable and tunable cantilever–mass system. The oscillations create contact separation between the triboelectric-active layers (i.e. fluorinated ethylene–propylene copolymer and screen-printed zinc oxide), which develop triboelectric waveforms. This voltage waveform is used for both sensing and powering mechanisms. At resonance, the device produces peak-to-peak voltage, short-circuit current, and power density of 25 V, 10 μ A, and 1.38 W m⁻², respectively. To measure the influence of change in cantilever properties, we varied the number of cantilevers and evaluated the sensor performance. The sensor is reliable with >99% accuracy in a broad frequency range of 0–400 Hz. The sensor exhibits a maximum sensitivity of 14 V g⁻¹ and can charge a 1 μ F capacitor to 2.75 V in <150 s. The sensor is further tested on a lab-scale vacuum pump with known (induced) faults to estimate the sensor's competence in detecting the machinery faults. Considering the market acceptability, the sensor is developed with established manufacturing techniques such as screen-printing, and laser cutting. This study hopes to bridge the lab-to-market gap for TENG-based (vibration) sensors.

Supplementary material for this article is available [online](#)

Keywords: vibration sensor, structural health monitoring, condition monitoring, single-electrode mode triboelectric device, lab-to-market

(Some figures may appear in color only in the online journal)

* Author to whom any correspondence should be addressed.

1. Introduction

Real-time and continuous condition monitoring of industrial machinery is one of the important tools that can save industries unplanned overhead costs by early detection of machinery faults, mitigating risks, and allowing for pro-active planning. There are several techniques for condition monitoring such as vibration monitoring, oil analysis, current signature analysis, infrared imaging, physical observations, etc [1–3]. Out of these, vibration pattern analysis-based condition monitoring is considered important because the vibration signatures of the machines are very early indicators of the failure of machines. Additionally, this technique provides multiple information such as running speed and bearing issues [4, 5] and can be remotely monitored. The vibration sensors currently employed in the industries are either piezoelectric-based sensors [6] or image-processing cameras [7]. These sensors/systems require a steady power supply or onboard battery management systems, which leads to other battery-related issues such as increased overhead costs, battery management systems, battery leakages, etc. These problems can be circumvented by employing self-powering vibration sensors.

Energy harvesting from ambient mechanical vibrations has been gaining a lot of attraction recently. In this direction, several energy harvesters have been reported electrostatic [8, 9], electromagnetic [10, 11], piezoelectric [12, 13], and triboelectric technologies [14, 15]. Triboelectric nanogenerators (TENG) have gained significant interest due to their cost-effectiveness and versatile device architectures. In TENG-based vibration sensors, the generated TENG voltage signal is employed as both sensing and powering signal.

The previously reported TENG-based vibration energy sensors could generate minimal power density except for the work of Hu *et al* [14, 16–18] which achieved the highest power density of 2.76 W m^{-2} . However, owing to the 3D spiral architecture's resonance, their device is limited to a narrow band operating frequency of 0–30 Hz. Additionally, most vibration energy harvesters [18–23] have employed secondary surface area (and in turn charge) enhancement techniques such as induction coupled plasma (ICP)-etched surfaces and electro-spinning to generate textures on the active surfaces.

In our proposed sensor, to address these challenges of narrow bandwidth and small output power, we have developed a novel, circularly supported, (multi)cantilever system encased in a robust outer body that can withstand high vibration amplitudes. We employed a screen-printed ZnO film and commercial fluorinated ethylene-propylene copolymer (FEP) as triboelectric-active layers on a single-electrode TENG architecture to free the vibrating element from electrical connections. The screen-printed film produces a grass-like surface texture without the need for additional enhancement techniques. The sensor produces an appreciable power density of 1.38 W m^{-2} at $1 \text{ M}\Omega$ load resistance and has a wide operating bandwidth of 0–400 Hz with >99% accuracy. The sensor generates a maximum sensitivity of $\sim 14 \text{ V g}^{-1}$. Furthermore, we tested the vibration sensor on an active pump to showcase the real-time applications. The sensor identified the operating speeds and detected the induced faults in the motor

operation, thereby proving its utility for condition-based monitoring. This study highlights that the proposed sensor can be used as a vibration sensor and a vibration energy harvester.

2. Experimental section

2.1. Fabrication of vibration sensor

Based on the function, the sensor can be divided into two major components: the mechanical and triboelectric systems. The mechanical system consists of structural components and vibrating components, as shown in figures 1(a) and (b). The structural components (i.e. the top and bottom covers, mass spacers, wiring spacers, and fasteners as indicated later in figures 3(b) and (d)) constitute the outer bodies (made of laser-cut acrylic blocks). The vibrating components consist of (a) a computerized numeric control (CNC)-machined sheet-metal part (0.25 mm thick aluminum sheet) and (b) a machined brass block. The triboelectric system consists of a commercial FEP sheet (0.1 mm thick) and screen-printed ZnO films cladded to the brass block and acrylic cover, respectively, as shown in figure 1(c).

2.2. Triboelectric system

A screen-printed ZnO film is used as the tribo-positive layer. The preparation of the tribo-positive layer is shown in figure 1(c). The ZnO paste is prepared first, and then the film is fabricated using the screen-printing technique. For paste preparation, a mixture of 50 wt% ZnO nano-powder, 45 wt% terpinol, and 5 wt% binders (ethylcellulose) was vigorously ground using a mortar and pestle for 15 min to form an agglomerate-free screen-printable paste. The prepared ZnO paste is screen-printed manually using a #180 mesh screen layer. A snap-off distance of 5–10 mm is used to produce a uniform, texture-free smooth surface during printing. A copper adhesive tape was used as a substrate, cleaned by using isopropyl alcohol, acetone, and deionized water (in that order) to eliminate all organic and inorganic contaminants from the surface before screen-printing. The printed oxide film is dried under an infrared lamp for approximately 2 h for the solvents to evaporate. The film obtained is 7 μm thick and inherently contains grass-like morphology. Further details can be found in the earlier report [24]. The adhesive in the copper facilitates assembling the ZnO film onto the acrylic cover.

2.3. Assembly

The vibration sensor is assembled in multiple stages. The top and bottom cover plates are cladded with a tribo-positive layer using thin, double-sided adhesive tape. The acrylic wiring spacer is glued to the top and bottom cover plate using chloroform to connect wires. Subsequently, the connecting wires are soldered onto the extended electrodes and routed via the narrow slit provided in the acrylic wiring spacer. The wires are glued to the acrylic covers using strong insulation tape to protect the electrical connections from mechanical failures. The

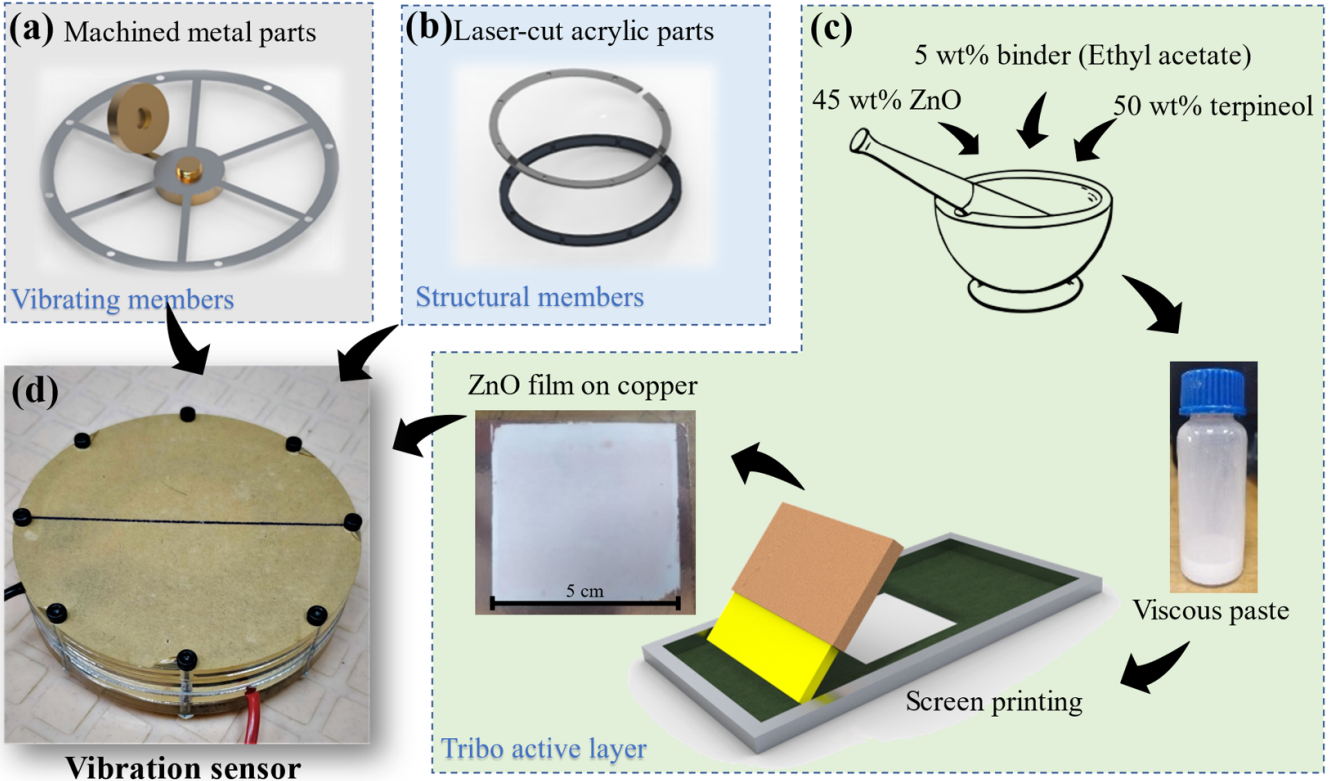


Figure 1. Overview of the vibration sensor. (a) Machined metal parts in the vibrating components of the sensor. (b) Laser-cut acrylic parts of the structural components of the sensor. (c) Preparation of triboelectric layer (ZnO) by using a screen-printing technique. (d) Complete assembly of the vibration sensor.

solder joints experience mechanical loads from the weight of the wire when the device is subjected to vibrations. For the final assembly, the acrylic cover (along with the tribo-positive layer, and wiring spacer and wires) is aligned with other layers (mass spacer, vibrating component, and seismic mass) and bolted with a M3 nut and bolt arrangement.

2.4. Lab testing

The vibration sensor is tested on a Fredrick 2185 vibration generator, as shown in figure 2. The sensor is mounted onto the vibration generator securely using superglue (cyanoacrylate). The vibration generator is excited using a function generator (AFG 3022c) and the device voltage output is captured using an oscilloscope (DPO 2014b). The oscilloscope has an input impedance of $10 \text{ M}\Omega$. The short circuit current is measured using a Keithley semiconductor parameter analyzer 4200s. An ADXL 335 accelerometer is used to measure the acceleration experienced by the vibration sensor when excited by the external vibration generator. A 2 mm thick aluminum sheet is placed at the bottom of the surface to ensure the vibrations are transmitted uniformly throughout the sensor while testing. For the case study, the sensor is mounted onto a 1/8th HP vacuum pump (GAST, model No. DOA-P725-BN, rated at 1440 rpm) using a thin layer of double-sided adhesive tape. A flat surface on the pump is cleaned with solvent, and then a uniform layer of adhesive tape is pasted on it. Subsequently, the sensor is positioned on the motor and secured

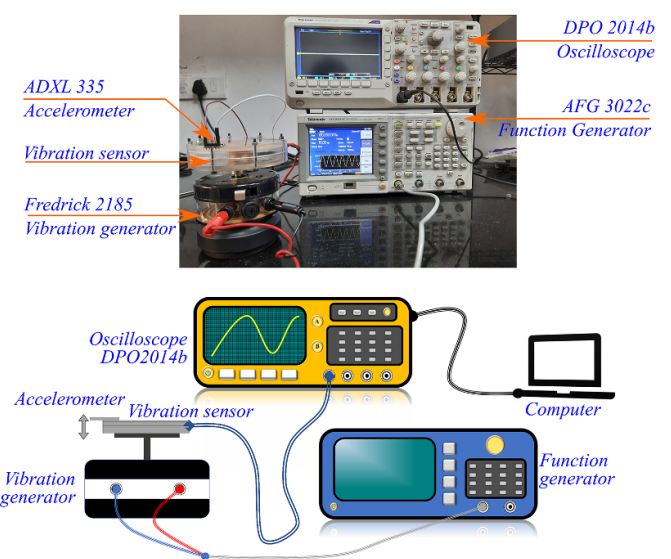


Figure 2. Experimental setup of the vibration sensor testing. The vibration sensor, along with the accelerometer, is mounted on the vibration generator. The vibration sensor data is captured via the oscilloscope DPO 2014b and recorded on a laptop. A suitable excitation vibration waveform is selected in the function generator AFG 3022c which then drives the vibration generator accordingly.

tightly with adhesive tape. To introduce artificial faults in the pump, a ‘loose foundation’ is chosen for study since it does not require any internal modifications. A standard acrylic spacer

of 5 mm, 7 mm, or 12 mm is placed below one of the legs to introduce imbalance in the system.

3. Results and discussion

The vibration sensor is a low aspect ratio (i.e. height/diameter ~ 0.48 as indicated in figure 3(d)) cylindrical structure with a (vibrating) aluminum layer sandwiched between rigid acrylic structural components. The low aspect ratio helps in reducing the center of gravity and increases the stability of the sensor. The cylindrical shape of the sensor helps in changing the number of beams in the vibrating component freely without affecting the symmetry. The circular shape can accommodate any number of equal length beams, which other shapes such as square or triangle or other polygons cannot offer. The proposed design is novel and scalable (i.e. the overall sensor dimensions can be customized to the specific application without compromising the device performance). Most importantly, it has ergonomically designed, generic architecture. It is easy to customize the sensor to targeted applications.

The detailed structure and assembly of the sensor are shown in figure 3. Figure 3(a) shows the final vibration sensor prototype with electrical wires coming out from the top and bottom TENG layers. Figure 3(b) shows the exploded view of the sensor with all the layers labeled. Figure 3(c) shows the vibration sensor without the top cover to reveal the arrangements of the layers. Figure 3(d) highlights the outer dimensions of the vibration sensor. Figures 3(a) and (c) are photographs of the fabricated prototype, while figures 3(b) and (d) are the digital twins generated using CREO software.

The seismic/proof mass comprises two $\phi 25$ mm circular disks and 5 mm thick brass blocks in the vibration sensor. It is fastened to the aluminum beams (obtained by CNC-machined aluminum sheet metal) using the inbuilt thread and hole arrangements. The FEP is mounted on the brass surfaces. The spacers are fabricated using laser-cut acrylic sheets and help in holding the aluminum sheet in place. The top and bottom outer covers are made of 6 mm thick laser-cut acrylic sheets. Screen-printed zinc oxide (SP-ZnO) is pasted on the inner surface of these top and bottom covers. The SP-ZnO layers are electrically connected and hence require enough space for the connecting wires to escape. Thus, a wiring spacer is included in the assembly. The wiring spacer has a narrow slit in its circumference. The wiring spacer is made of a 2 mm thick acrylic sheet. The mass spacer is included to provide relief for the brass. It has the same thickness as the brass (i.e. 5 mm). All the individual layers are assembled using a prestressed M3 nut and bolt arrangement, which keeps the individual layers in place. Once all parts in the sensor are assembled, the gap between the FEP and the SP-ZnO (after deducting the thickness of all the adhesives used) is in the range of 0.25–0.5 mm.

The outer dimensions of the sensor are 105 mm diameter and 50 mm height, as shown in figure 3(d). The total weight of the sensor and the weight of the suspended brass is 192 g and 40 g, respectively. The screen-printed ZnO film is 7 μm thick with 1 μm roughness [24, 25]. The triboelectric-active overlap area is 490.87 mm^2 (25 mm diameter).

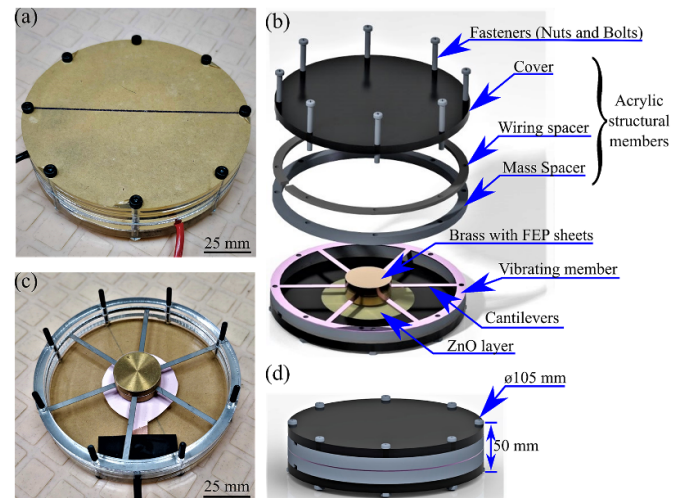


Figure 3. Vibration sensor overview. Panels: (a) the complete assembly of the vibration sensor prototype, (b) exploded view of the vibration sensor with parts labeled, (c) anatomy of the vibration sensor shown by removing the top acrylic covers, (d) the computer-aided design (CAD) model of the entire assembly.

When the sensor is mounted on the external casing of any vibrating machinery, the entire sensor gets excited due to the transmitted vibrations via the mounting base. When transmitted to the brass block, these vibrations are magnified since it is suspended by an elastic cantilever beam structure. The CNC-machined aluminum beams along with the seismic mass are treated as a cantilever beam system (a spring-mass system connected parallelly). The circular cantilever beam component with seismic brass mass acts as a vibration amplifier, and equations S1–S4 in table S1 (available online at stacks.iop.org/MST/33/075115/mmedia) gives its corresponding governing equations [26].

The geometric parameters of the beams such as their length, width, thickness, and the number of beams play a vital role in determining the cantilever system's static and dynamic deflections (and harmonic response). These parameters can be used to tune the natural frequency of the vibrating component. The influence of these geometric parameters on the natural frequency has been plotted using equations S1–S4 and further elaborated in section 1 of the supplementary material.

The effect of geometric parameters (beam length, beam width, beam thickness, and the number of beams) on static deflections are shown in figure 4. From figure 4(a), it is observed that the static deflection keeps increasing as the beam length increases. Figures 4(b) and (c) shows that the net static deflection reduces as the beam width and thickness increase. From equation S1, it is observed that the static deflection of the beam is inversely proportional to its I [27]. For a rectangular beam $I = wt^3/12$, where w is the breadth of the beam and t is the thickness of the beam. Upon back substituting into equation S1, the observed changes of figure 4 are attributed to the correlations of the static deflection with geometric parameters i.e. static deflection is proportional to t^3 , inversely proportional to w , and inversely proportional to I .

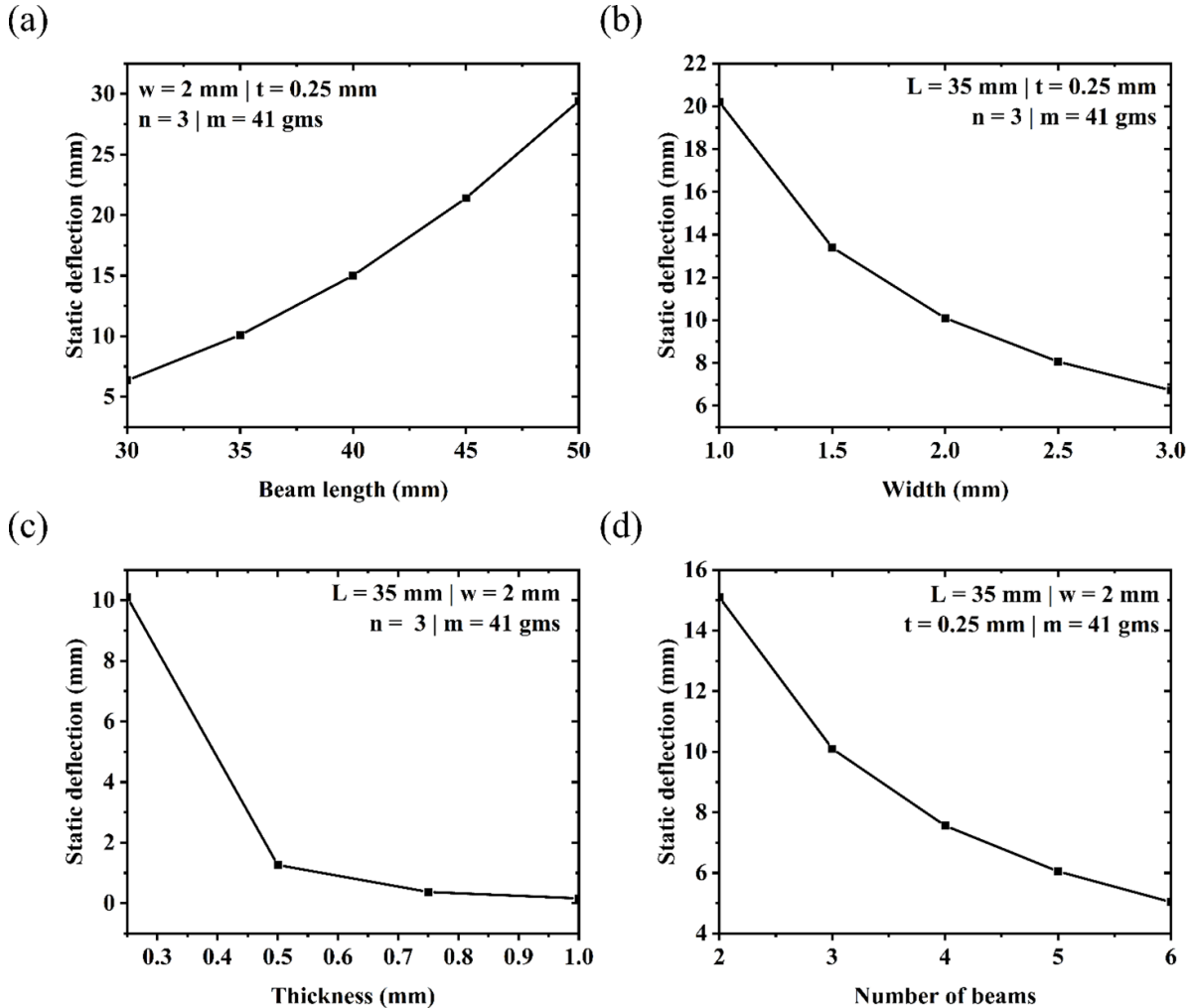


Figure 4. Effect of geometric parameters on the static deflection of the vibration sensor: (a) effect of beam length, (b) effect of width, (c) effect of thickness of beam, and (d) effect of the number of beams.

While from figure 4(d), it is observed that as the number of beams increases, the static deflection reduces. As the beams are connected in parallel configurations, as the number of similar beams increases, the net stiffness in the cantilever system increases proportionately. These geometric parameters can be tuned suitably to scale up the model or miniaturize using isotropic linear elastic beam material (aluminum). This allows for the tunability of the sensor to the desired geometric constraints. Here, the static deflection is governed by the maximum allowable gap in the sensor (0.25 mm) and is selected to keep the maximum stresses developed in the component within the elastic limit of 70 GPa [28].

Depending upon the input mechanical excitation frequency, the dynamic vibration amplitude of the brass block varies (as shown in figure 5(a)). The brass block deflection reaches its maximum at resonance. Since the seismic brass mass is constrained to deflect within the allowable gap, when the deflection crosses the threshold of the permissible gap, the brass comes in contact with the top and bottom covers and triggers a triboelectric signal. The generated triboelectric signal is thus dependent on the input mechanical frequency (as shown in figure 5(b)).

It is observed that the generated triboelectric voltage waveform does not show a peak at the same position as the harmonic response from the theoretical calculations of the vibrating component (i.e. figure 5(a)). This is associated with the fact that the harmonic response does not account for the reaction forces developed at the interfaces when the brass block collides and creates secondary vibrations. Additionally, the triboelectric voltage waveform is the net response of the entire vibration sensor assembly, while the harmonic response is evaluated for the aluminum vibrating component in isolation, without any support structures. The triboelectric voltage waveform shows three peaks (at 18.6 Hz, 31.1 Hz, and 43.3 Hz), as shown in figure 5(b), which correspond to the three resonant points of the entire assembly.

3.1. Triboelectric signal generation

When two dissimilar materials come in contact and separate, owing to the difference in their electron affinities, the direction of surface charges' transfer is from weaker to stronger electron affinity [29, 30]. This charge transfer makes the two surfaces electrically charged with opposite polarity. These sheets of

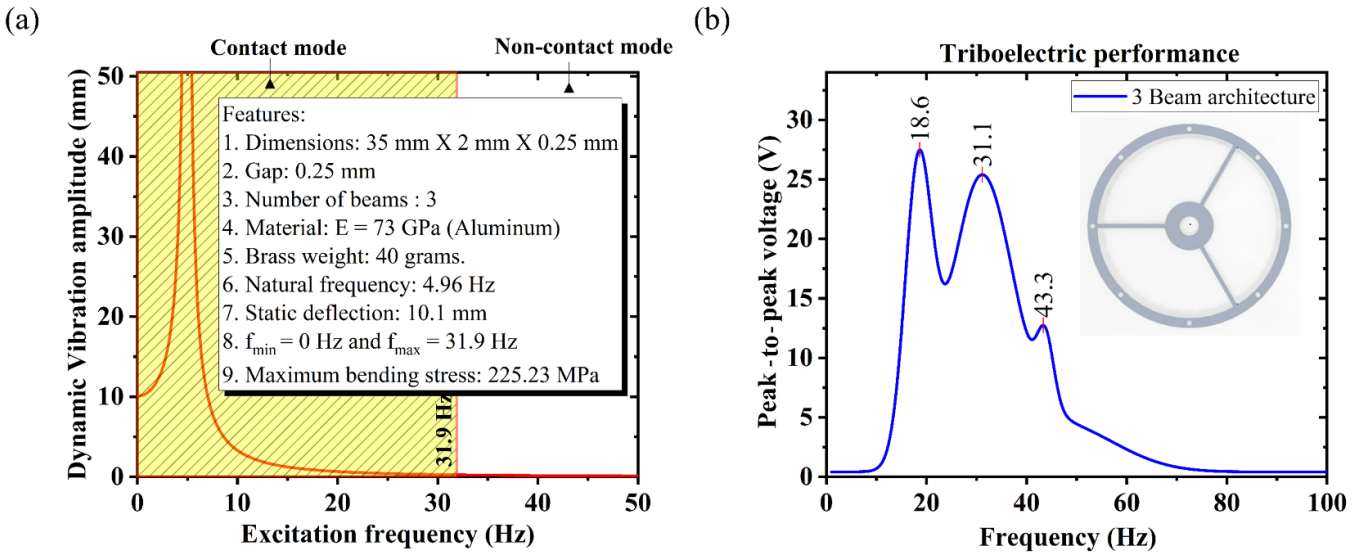


Figure 5. (a) Harmonic response of three-beam configuration vibration sensors and (b) effect of input mechanical frequency on triboelectric performance of a three-beam configuration vibration sensor Inset in (b) shows the three beams vibrating component.

charges create an electric field around them. As a result, the electric field polarizes the backing electrodes, which causes a flow of electrons in the external circuit constituting a triboelectric signal. When the materials come back in contact, the charged surfaces coincide, and hence the established electric field collapses.

Consequently, the polarity in the backing electrode causing the reverse flow of charges in the external circuit is nullified [31–37]. However, in the case of single-electrode mode [38, 39], one of the backing electrodes is not connected electrically, and the other surface is left free from electrical connections. This configuration benefits from electrically connecting only the stationary electrode, and the moving electrode can be left free. Here in the single-electrode mode of operation, a remote electrode could be used as a reference potential, or two TENG devices could be coupled in tandem, and both of the devices could be used as a reference for one another.

Our vibration sensor has two single-electrode mode TENG devices placed on the top and bottom of the vibrating brass block and they work in tandem. The TENG device architecture (i.e. placement of the active layers) and intermittent vibration steps are depicted clearly in figure 6 (and figure 3(b)). Each pair of ZnO-FEP active layer constitute an individual single-electrode mode TENG device. The two TENG devices are placed on the top and bottom of the brass block (brass and acrylic interfaces as shown in figure 6(b)–(i)). The backing electrodes are placed only behind the ZnO layers (mounted on the acrylic covers), and the FEP (mounted on the brass) is not electrically connected. The TENG voltage is captured between the backing electrodes of the top and bottom ZnO layers. Connecting to the FEP electrically causes uncertainty in the harmonic response of the brass block because of the weight and stiffness of the wires. Hence an untethered FEP layer is employed, which allows for predictable vibrations of the brass block. The detailed electrical connections are shown in figures 6(b)–(ii) and (b)–(iv). The generated charges disappear when the FEP

hits the bottom ZnO TENG layer (interfaces). Hence, there will be a potential difference between the top and bottom backing electrodes. This causes charges to flow between them. Now, when the brass block moves up, the bottom TENG layers are charged again. This will perturb the equilibrium setup and causes the reverse flow of charges to bring back the equilibrium. Figure 6(i)–(iv) shows the detailed triboelectric stages step by step.

3.2. Triboelectric performance evaluation of the vibration sensor

The triboelectric performance of the vibration sensor varies as a function of geometric parameters such as beam length, beam width, beam aspect ratio, etc. To understand the effects of geometric parameters on the system performance, we have selected the number of cantilever beams as a variable while retaining other geometric parameters constant. The TENG system performance parameters are evaluated experimentally. We varied the number of cantilever beams from three to six. We observed that, as the number of beams increases, the peak-to-peak voltage, current, transfer charges, and the maximum power drop continuously (as shown in figures 7(a)–(d)). The three-beam architecture showcased the maximum TENG system performance under the tested conditions and developed a peak-to-peak voltage of 25 V, a short circuit current of 10 μ A, and 40 nC of charges. The device produces a maximum power of 680 μ W at 18 Hz or 1.38 W m⁻² (obtained by normalizing the maximum power with the active overlap area of 490.87 mm²). These performance parameters are comparable to the previously reported values [24, 40]. Here, it is observed that the maximum power decreases with an increase in the number of beams, but the TENG device output impedance remains the same at 1 M Ω . This is attributed to the system's internal architecture (i.e. the active overlap area, the thickness of the tribo-active layers, and electrical connections), which

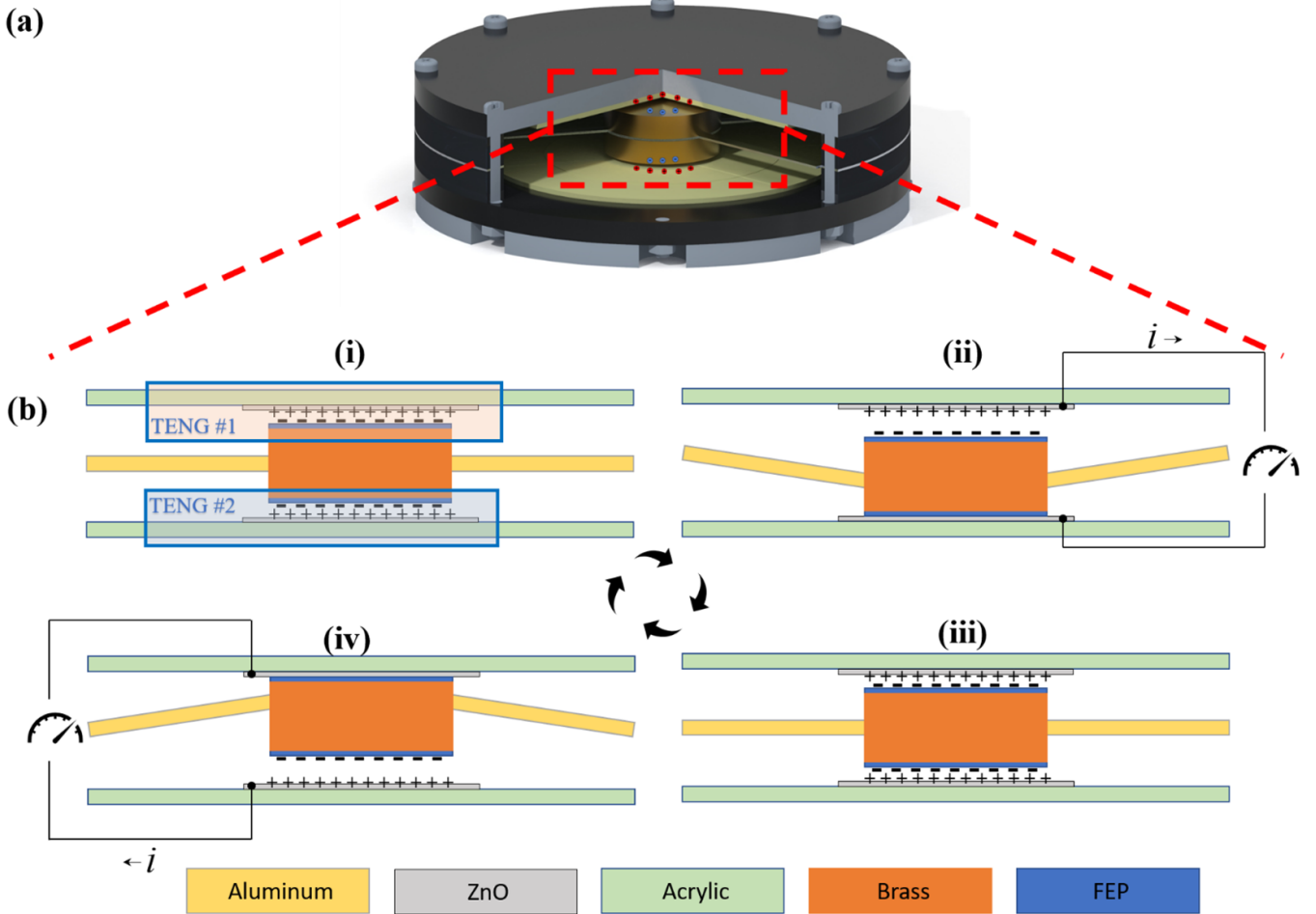


Figure 6. Working principle of the vibration sensor along with detailed intermediate steps. (a) shows the sectional view of the vibration sensor highlighting the charge accumulation on the active layers and (b) step by step movements of brass block resulting in charge generations on active layers. (i) The two TENG devices are highlighted along with the decorated static charges on the interface surfaces of the active material, (ii) the proof mass is in the bottom-most position and contact is established in the bottom TENG device, causing the static charges to disappear, (iii) the brass block is moving in an upward direction thus both the TENG devices are in the separated position with surface charges present on both the TENG devices, (iv) the brass block has travelled to the topmost position, making contact in the top TENG device causing the static charges to disappear.

does not change with the number of beams. To evaluate the energy harvesting performance of the device, the vibration sensor is excited at 18 Hz, and a $1\ \mu\text{F}$ capacitor is charged from the TENG device output using the circuit shown in figure 7(e). The charging curves (shown in figure 7(f)) showed that the three-beam capacitor charged the capacitor to a higher voltage (2.78 V) while the six-beam sensor charged the same capacitor to a lesser voltage (0.92 V) in the same duration of 150 s. The capacitor charging curves also followed the same trend as that of the peak-to-peak voltage. (i.e. the capacitor saturation voltage reduced with an increase in the number of beams). This is expected since the net voltage keeps dropping with the increase in the number of beams.

3.3. Frequency-dependent response of the sensor

The TENG performance of the vibration sensor is dependent on the excitation frequency. This is associated with the fact that the vibration amplitude of the brass block is a function of input frequency as per equation (5) in SI.

The dynamic harmonic response of the system is shown in figure 8(a). The graphs show peaks at 18.6 Hz, 31.1 Hz, and 43.3 Hz, which are its eigenmodes of vibrations. The peaks are prominent for three-beam architecture, and as the number of beams is increased, (a) the peak-to-peak voltage magnitude keeps reducing, and (b) the first peak (centered at 18.1 Hz) is fixed while the second and third peaks are shifting in either direction. This is attributed to the increase in overall stiffness in cantilevers when the number of beams is increased [27]. The increases in stiffness also reduce the interface forces, which subsequently reduces the voltage produced [29]. Also, as the stiffness is changed, the vibration characteristics vary. This causes a shift in the peak position of the eigenmodes [41]. After the excitation frequency crosses the threshold of contact to a non-contact mode of operation (explained in figure 5), the voltage magnitude falls rapidly, and the waveform converts to pure sinusoidal, similar to a capacitive gyroscope designed to be operating in a non-contact mode [42]. The instances of the voltage waveforms of the vibration sensor excited at different vibrations are shown in figures 8(b) and (d). This

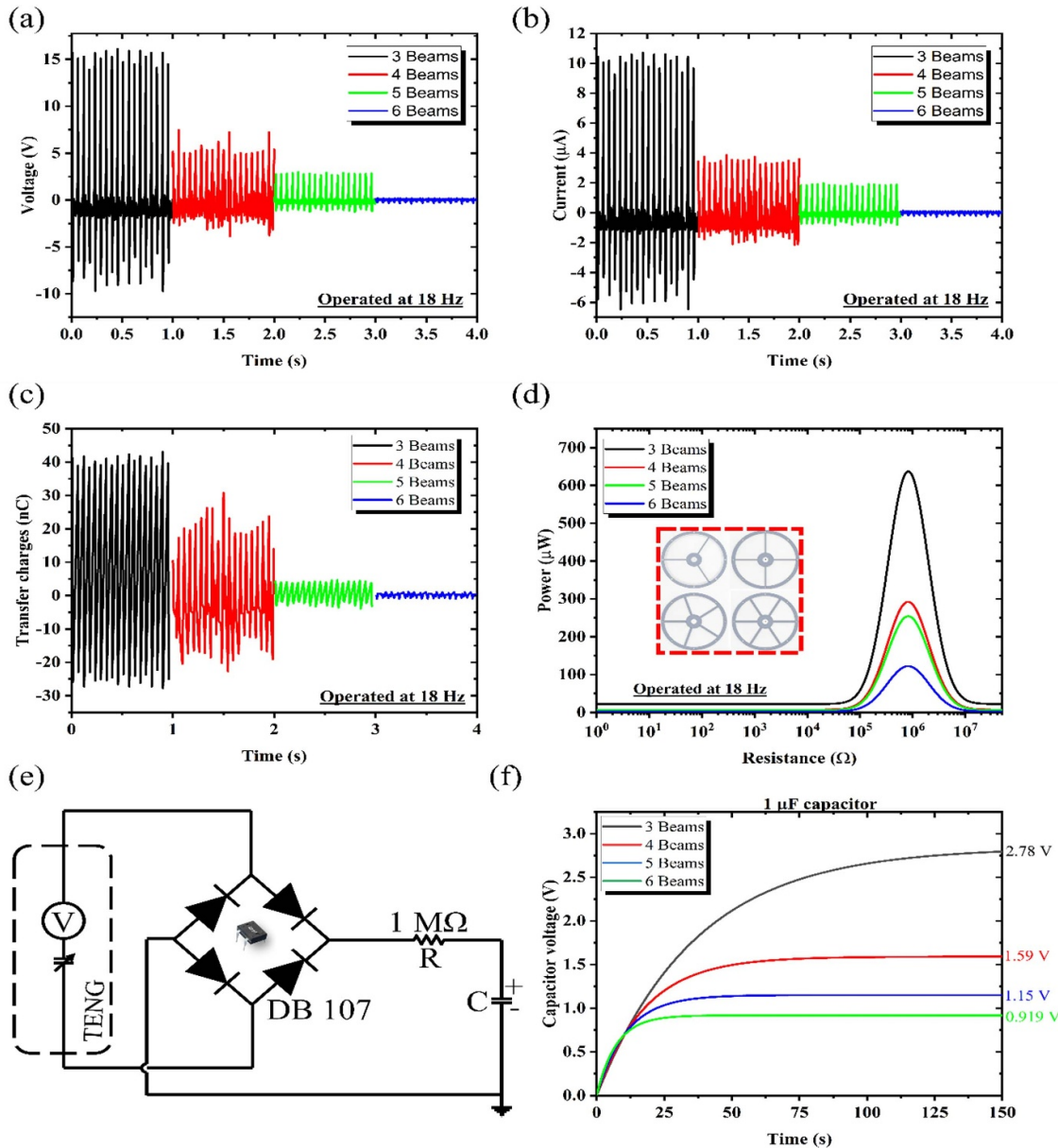


Figure 7. Triboelectric performance of the vibration sensor: (a) generated voltage, (b) short circuit current; (c) transferred charges in the external circuit, (d) load matching experiment to evaluate the maximum power delivered by the system. Inset showing the vibrating component with three, four, five, and six beams respectively, (e) capacitor charging circuit, (f) capacitor charging curves for the various number of beams.

trend is followed in the maximum power delivered by the system as well i.e. as the operating frequency is increased, the maximum power delivered by the system reduces, as shown in figure 8(c).

From figure 8(b), it is observed that the device produces a maximum peak-to-peak voltage of 25 V for three-beam configurations at 18 Hz. The voltage waveform is asymmetric, and the generated voltage amplitude is relatively more significant on the positive side of the graph and is somewhat smaller on the negative part of the graph. This indicates that the voltage generation is asymmetric in nature and the bottom tribo-pair produces a higher voltage than the top electrode pair. This is because the interface loads are higher at the bottom electrode pair than at the top pair when the brass block is traveling in the downward direction; the net acceleration is the summation

of vibration-induced acceleration and standard earth gravity, but when the brass is moving in the upward direction, the net acceleration is the difference between the two. Hence the net interface force at the bottom tribo-pair is larger than the top tribo-pair. This is proven by the erosion patterns developed on the ZnO films. The bottom ZnO is eroded more than the top ZnO layer, as shown in figure S2 in the supplementary material.

To evaluate the operating band of the sensor, the sensor is then tested on the vibration generator, and the input mechanical vibrations are controlled using a function generator (AFG 3022c). The input frequencies are varied from 1 Hz to 400 Hz (generic operating frequency range for conventional pieces of machinery). The generated voltage waveform is subjected to Fourier transformation (FFT). The FFT operation identifies all

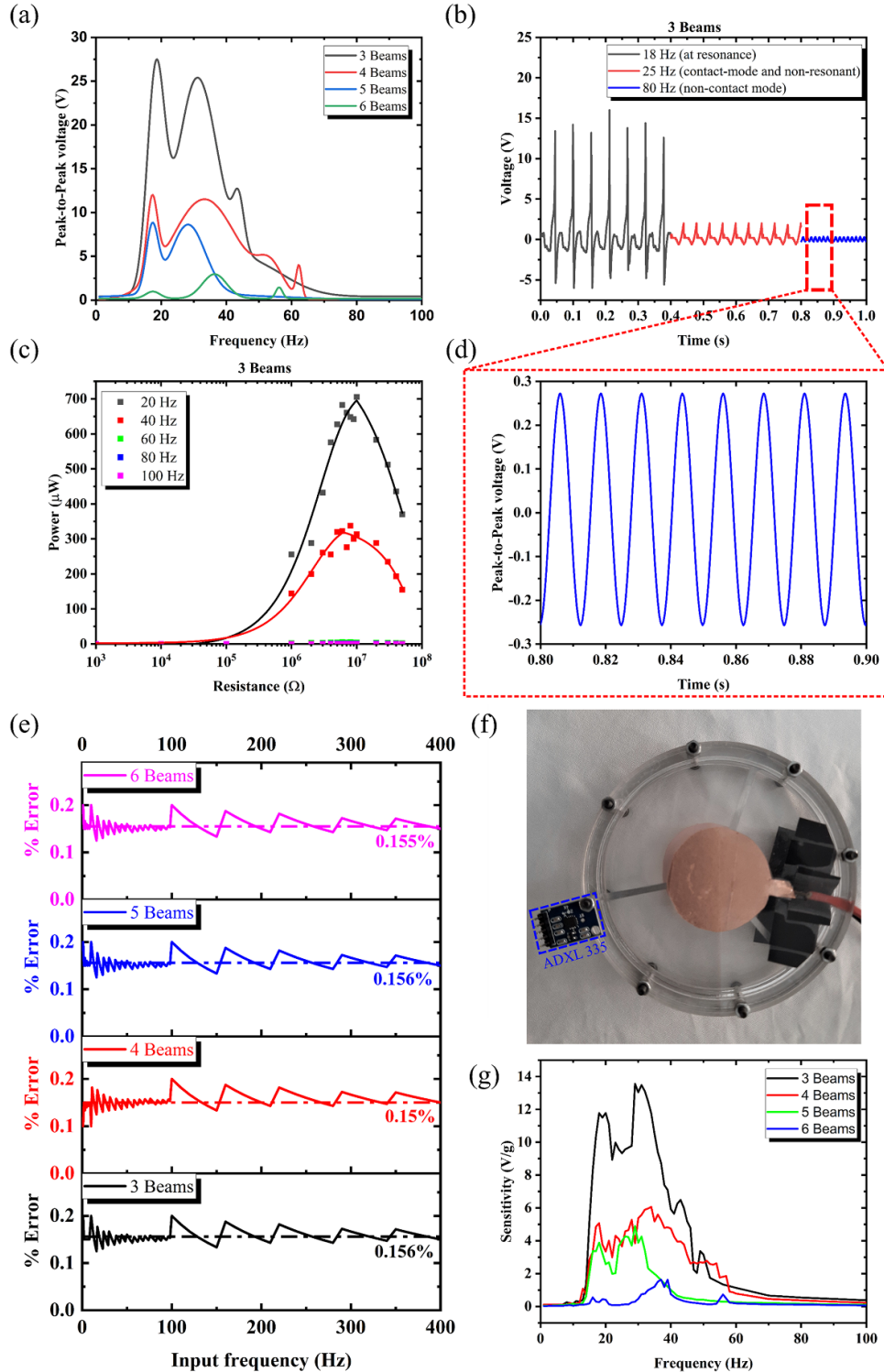


Figure 8. Harmonic response of the vibration sensors: (a) change in peak-to-peak voltage of the vibration sensor for the various number of beams in the frequency domain, (b) time-domain voltage waveform of the vibration sensor for different excitation frequencies, (c) maximum power of the three-beam vibration sensor evaluated at different mechanical excitation frequencies, (d) zoomed-in image of the voltage waveform at the non-contact mode of operation, (e) percentage error of the vibration sensors showing similar medians for three, four, five, and six beams architecture, (f) vibration sensor mounted along with the ADXL 335 for evaluating the magnitude of g on the vibration sensor, (g) sensitivity of the vibration sensor evaluated with the help of a standard accelerometer (ADXL 335).

the constituent frequencies the voltage waveform contains, and from this list, as a standard practice, the frequency closest to the input frequency is selected as the output frequency.

From the input and output frequency, the percentage error is evaluated [43], and the plots obtained are shown in figure 8(e). It is observed that the sensor's output has a minimum error of

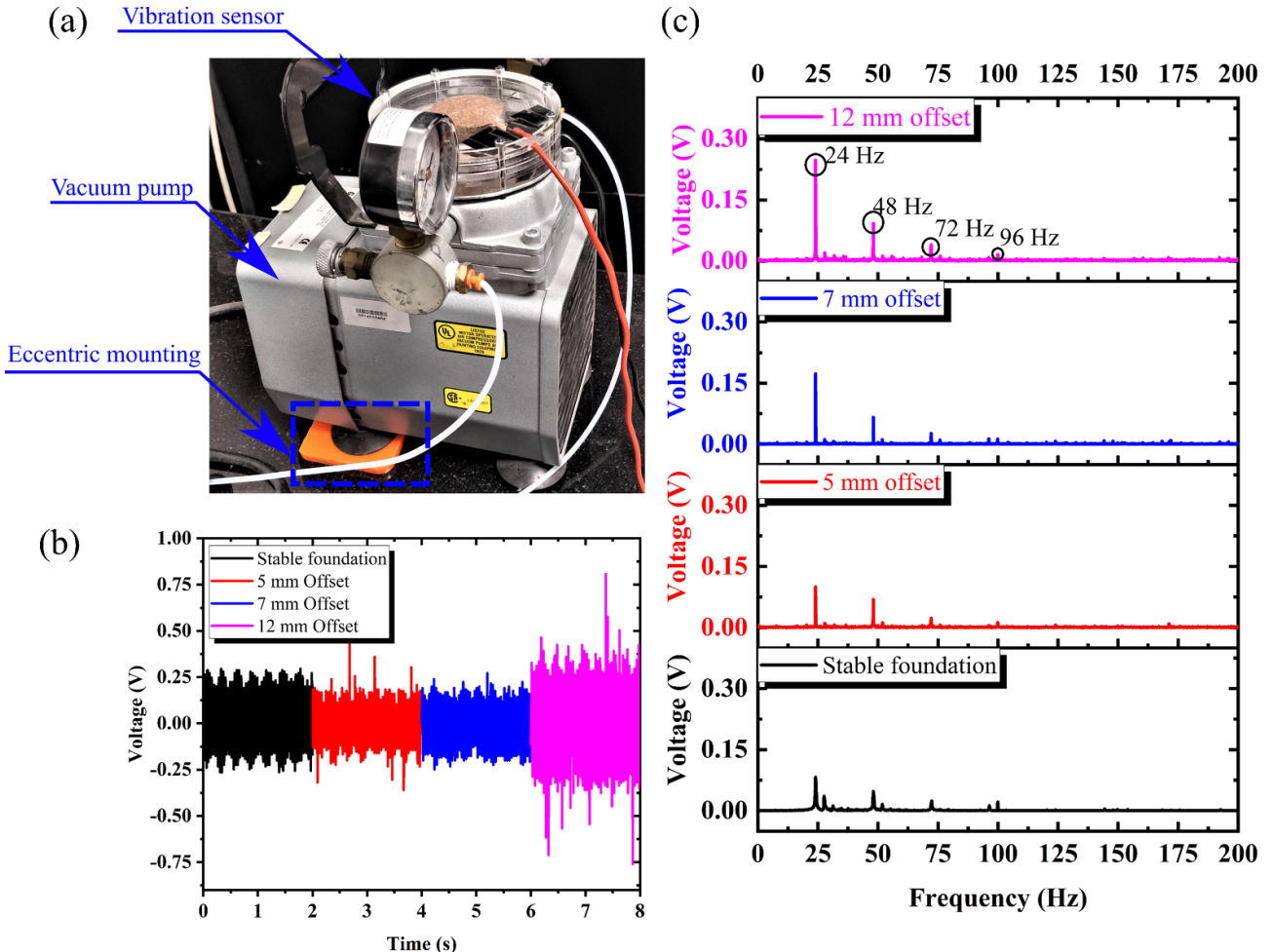


Figure 9. Condition monitoring for a vacuum pump using the vibration sensor: (a) sensor mounted on a vacuum pump mounted with an unstable foundation, (b) generated voltage waveform of the vibration sensor (vibration sensor mounted on varying degrees of eccentricity at the foundation), (c) FFT spectrum of the voltage waveform of the vibration sensor mounted on a vacuum pump with a loose foundation.

0.156% for all architectures and the plots exhibit a sawtooth-like waveform. In the frequency domain of 1–100 Hz, the percentage error is negligible (<0.1%) since the device is operating in a contact mode of operation. In the later regime, i.e. from 100 Hz to 400 Hz, the percentage error increases but still retains the median of 0.156%. This relatively low error level indicates that the vibration sensor can be used as a linear vibration sensor in the domain of 1–400 Hz with ~99.85% accuracy applicable to most conventional electrical machinery.

To gauge the vibration sensor's sensitivity, the vibration sensor is tested along with a commercial accelerometer (ADXL 335), as shown in figure 8(f). From the accelerometer data, we conclude that the vibration sensor experiences a maximum acceleration of ≈ 3 g; calculated sensitivity of the sensor is plotted in figure 8(g). The sensitivity is obtained by normalizing the peak-to-peak voltage of the vibration sensor to the instantaneous acceleration due to gravity (recorded from the accelerometer). The acceleration data recorded from the ADXL 335 is explained in section S3 and plotted in figure S3. From the graph (figure 8(g)), it is observed that the sensitivity of the vibration sensor is maximum with three-beam architecture (a sensitivity of 14 V g^{-1}) and reduces with the

increase in the number of beams. The six-beam architecture shows the least sensitivity of 1.5 V g^{-1} . This is mainly because the three-beam architecture shows the highest generated voltage of all the architectures. This could be generalized as the sensitivity is maximum when the vibration sensor produces a maximum voltage which is again inversely proportional to the stiffness of the vibrating component.

3.4. Condition monitoring of the motor

To demonstrate the vibration sensor's usage for condition monitoring applications, we tested the vibration sensor in a controlled environment by introducing artificial faults in the machinery. We introduced 'loose foundation' as a fault, as it does not require internal modifications to the pump. The loose foundation is introduced by placing acrylic blocks of standard thickness below one of the legs, thus introducing an imbalance on the rotating shaft. When one of the legs is elevated, the rotating components experience the force imbalance as its center of gravity shifts from the designed locus. This induces vibrations in the support bearings/structures at the same speed

as pump operation. Thus, the amplitude of the frequency corresponding to the rated capacity in the FFT spectrum keeps growing with an increase in offset height.

We employed the three-beam architecture vibration sensor as a testing sample since its sensitivity is the highest among the tested configurations. Figure 9(a) shows the vibration sensor mounted on the vacuum pump along with the acrylic block placed below a leg. Figure 9(b) shows the time domain voltage waveform of the vibration sensor when mounted on the vacuum pump operating at full capacity. Figure 9(c) shows the FFT analysis of the recorded voltage data with different height offsets. The FFT spectrum shows sharp peaks corresponding to the system's rated capacity (24 Hz), indicating that the vacuum pump is operating at rated capacity, which indicates no issues with the pump power input or the bearing systems. These observations show that the pump is in good condition and does not require any maintenance imminently. When the offset is introduced in the pump, as expected, the amplitude of the 24 Hz frequency (and its eigenmodes) keeps growing. The amplitude gain in the FFT spectrum is depicted in figure 9(c). The signal achieved a maximum amplification of 9.6 dB (evaluated using equation (1) [24]) when a 12 mm offset was introduced.

$$dB = 20 \times \log_{10} \left(\frac{N_1}{N_2} \right) \quad (1)$$

where N_1 and N_2 are the final and reference signal magnitudes.

Here, it is observed that the sensor did not require any specialized mounting requirements such as magnetic mounting or mounting on specific locations on the housings. The sensor was mounted with little effort by using commercially available, double-sided adhesive tape. The sensor captured the operating frequency accurately. Since the sensor is proven to be self-powering from the capacitor charging experiments, as shown in figure 7(f), this enables the implementation of the sensor with battery management circuits.

4. Conclusions

In this paper, we have demonstrated a self-powering vibration sensor working on a cantilever-based, single-electrode mode, contact separation-type TENG. The vibration sensor is highly tuneable, scalable, and can be made robust to meet the target application requirement. The changes observed in the frequency response prove that the sensor could be tuned without major design changes (i.e. a stiffer cantilever, say six-beam architecture, could be used with large amplitude vibrations and a relatively less stiff cantilever, say three-beam architecture, be used for softer applications) without losing the sensing accuracy. This passive sensor is designed to capture the harmonic vibrations produced by the machinery body, which contain useful information about the system's health. During sensor development, cost-effectiveness and large-scale production are given paramount importance, which could ease large-scale implementation. The sensor can act as a powerful node in the vast network of Internet of Things (IoT)-based structural health monitoring (SHM) and condition monitoring (CM)

techniques owing to its versatile robust design, self-powering passive nature, and large operation bandwidth (0–400 Hz), which covers most conventional electrical machinery. As the vibration sensor can sufficiently charge a capacitor (1 μ F capacitor to 2.75 V in 150 s), the sensor could make use of the generated signal for both sensing and powering mechanisms, making it a self-powering vibration sensor. The critical part of the sensor is made of linear elastic material, which makes the sensor tuneable. Here, the sensor enclosures have been fabricated using acrylic for lab-scale experiments, which can be replaced with any appropriate materials as the application demands. The sensor could be retrofitted for any of the specialized requirements if needed.

The sensor recognized the pump operations without errors, indicating that the sensor design is sufficiently developed to be employed in real-time applications. The vibration signature of the machinery captured via the vibration sensor is filled with information (natural frequency, operating speeds, etc.). By introducing advanced machine learning (ML) and artificial intelligence (AI) algorithms, the vibration sensor could be an irreplaceable data source of the known issues and by training ML and AI algorithms to monitor these changes in the signal. Continuous real-time condition monitoring could be easily automated. These types of automation can help detect predictable defects in machinery and reduce unplanned downtime, which could be helpful in the long run.

Data availability statement

The data that support the findings of this study are available upon reasonable request from the authors.

Acknowledgments

The authors would like to acknowledge the TCTD lab and Tinkerers' lab at IITB for their support towards prototyping. The authors are grateful for the technical guidance provided by Professor Siddhartha Tallur.

Funding

This work is supported by the Government of India (RD/0119-DSTIM00-007), the Indian Space Research Organization (ISRO) (RD/0119-ISROC00-018), and partially supported by the Department of Science and Technology.

ORCID iD

Dipti Gupta  <https://orcid.org/0000-0003-3252-3407>

References

- [1] Henriquez P, Alonso J B, Ferrer M A and Travieso C M 2014 Review of automatic fault diagnosis systems using audio and vibration signals *IEEE Trans. Syst. Man, Cybern. Syst.* **44** 642–52

- [2] Wu H, Wang Y and Yu Z 2016 *In situ* monitoring of FDM machine condition via acoustic emission *Int. J. Adv. Manuf. Technol.* **84** 1483–95
- [3] Touret T, Changenet C, Ville F, Lalmi M and Becquerelle S 2018 On the use of temperature for online condition monitoring of geared systems—a review *Mech. Syst. Signal Process.* **101** 197–210
- [4] Glowacz A and Glowacz Z 2016 Diagnostics of stator faults of the single-phase induction motor using thermal images, MoASoS and selected classifiers *Meas. J. Int. Meas. Confed.* **93** 86–93
- [5] Kumar K V 2009 Fuzzy logic based fault detection in induction machines using lab view *J. Comput. Sci.* **9** 226–43
- [6] Kobayashi T, Okada H, Masuda T, Maeda R and Itoh T 2011 A digital output accelerometer using MEMS-based piezoelectric accelerometers and arrayed CMOS inverters with satellite capacitors *Smart Mater. Struct.* **20** 065017
- [7] Chen J G, Davis A, Wadhwa N, Durand F, Freeman W T and Büyüköztürk O 2017 Video camera-based vibration measurement for civil infrastructure applications *J. Infrastruct. Syst.* **23** 1–11
- [8] Tashiro R, Kabe N, Katayama K, Ishizuka Y, Tsuboi F and Tsuchiya K 2000 Development of an electrostatic generator that harness the motion of a living body *JSME Int. J. C* **43** 916–22
- [9] Naruse Y, Matsubara N, Mabuchi K, Izumi M and Suzuki S 2009 Electrostatic micro power generation from low-frequency vibration such as human motion *J. Micromech. Microeng.* **19** 094002
- [10] Wang D A and Chang K H 2010 Electromagnetic energy harvesting from flow induced vibration *Microelectronics J.* **41** 356–64
- [11] Arroyo E, Badel A and Formosa F 2013 Energy harvesting from ambient vibrations: electromagnetic device and synchronous extraction circuit *J. Intell. Mater. Syst. Struct.* **24** 2023–35
- [12] DuToit N E and Wardle B L 2007 Experimental verification of models for microfabricated piezoelectric vibration energy harvesters *AIAA J.* **45** 1126–37
- [13] Chen G, Meng Q, Fu H and Bao J 2013 Development and experiments of a micro piezoelectric vibration energy storage device *Mech. Syst. Signal Process.* **40** 377–84
- [14] Hu Y, Yang J, Jing Q, Niu S, Wu W and Wang Z L 2013 Triboelectric nanogenerator built on suspended 3d spiral structure as vibration and positioning sensor and wave energy harvester *ACS Nano* **7** 10424–32
- [15] Liang Q, Zhang Z, Yan X, Gu Y, Zhao Y, Zhang G, Lu S, Liao Q and Zhang Y 2015 Functional triboelectric generator as self-powered vibration sensor with contact mode and non-contact mode *Nano Energy* **14** 209–16
- [16] Wu Z, Zhang B, Zou H, Lin Z, Liu G and Wang Z L 2019 Multifunctional sensor based on translational-rotary triboelectric nanogenerator *Adv. Energy Mater.* **9** 1901124
- [17] Xu M, Wang P, Wang Y C, Zhang S L, Wang A C, Zhang C, Wang Z, Pan X and Wang Z L 2018 A soft and robust spring based triboelectric nanogenerator for harvesting arbitrary directional vibration energy and self-powered vibration sensing *Adv. Energy Mater.* **8** 1702432
- [18] Wang S, Niu S, Yang J, Lin L and Wang Z L 2014 Quantitative measurements of vibration amplitude using a contact-mode freestanding triboelectric nanogenerator *ACS Nano* **8** 12004–13
- [19] He Q, Wu Y, Feng Z, Sun C, Fan W, Zhou Z, Meng K, Fan E and Yang J 2019 Triboelectric vibration sensor for a human-machine interface built on ubiquitous surfaces *Nano Energy* **59** 689–96
- [20] Zhang B et al 2017 Self-powered acceleration sensor based on liquid metal triboelectric nanogenerator for vibration monitoring *ACS Nano* **11** 7440–6
- [21] Park J Y, Salauddin M and Rasel M S 2019 Nanogenerator for scavenging low frequency vibrations *J. Micromech. Microeng.* **29** 053001
- [22] Chen J and Wang Z L 2017 Reviving vibration energy harvesting and self-powered sensing by a triboelectric nanogenerator *Joule* **1** 480–521
- [23] Salauddin M, Toyabur R M, Maharjan P, Rasel M S, Cho H and Park J Y 2019 Design and experimental analysis of a low-frequency resonant hybridized nanogenerator with a wide bandwidth and high output power density *Nano Energy* **66** 104122
- [24] Hosangadi Prutvi S, Meti S, Bhat U K and Gupta D 2021 Triboelectric effect based self-powered compact vibration sensor for predictive maintenance of industrial machineries *Meas. Sci. Technol.* 1–5
- [25] Kartikay P, Yella A and Mallick S 2020 Binder-solvent effects on low temperature-processed carbon-based, hole-transport layer free perovskite solar cells *Mater. Chem. Phys.* **256** 123594
- [26] Hibbeler R C 2011 *Mechanics of Materials* (Hoboken, NJ: Pearson) (<https://doi.org/10.1016/j.mechmat.2010.12.004>)
- [27] Timoshenko S 1940 *Strength Of Materials* (New York: D. Van Nostrand Company)
- [28] Scari S, Pockszewnicki B C, Junior J L, Americo P and Magalhaes A 2014 Stress-strain compression of AA6082-T6 aluminum alloy at room temperature *J. Struct.* **2014** 387680
- [29] Seol M L, Lee S H, Han J W, Kim D, Cho G H and Choi Y K 2015 Impact of contact pressure on output voltage of triboelectric nanogenerator based on deformation of interfacial structures *Nano Energy* **17** 63–71
- [30] Lowell J and Rose-Innes A C 1980 Contact electrification *Adv. Phys.* **29** 947–1023
- [31] Dhakar L 2017 *Triboelectric Devices for Power Generation and Self-Powered Sensing Applications* (Berlin: Springer)
- [32] Davies D K 1969 Charge generation on dielectric surfaces *J. Phys. D: Appl. Phys.* **2** 1533
- [33] Lowell J and Truscott W S 1986 Triboelectrification of identical insulators. I. An experimental investigation *J. Phys. D: Appl. Phys.* **19** 1273–80
- [34] Wang Z L 2013 Triboelectric nanogenerators as new energy technology for self-powered systems and as active mechanical and chemical sensors *ACS Nano* **7** 9533–57
- [35] Niu S, Wang S, Lin L, Liu Y, Zhou Y S, Hu Y and Wang Z L 2013 Theoretical study of contact-mode triboelectric nanogenerators as an effective power source *Energy Environ. Sci.* **6** 3576
- [36] Niu S, Liu Y, Wang S, Lin L, Zhou Y S, Hu Y and Wang Z L 2013 Theory of sliding-mode triboelectric nanogenerators *Adv. Mater.* **25** 6184–93
- [37] Jiang T, Chen X, Yang K, Han C, Tang W and Wang Z L 2016 Theoretical study on rotary-sliding disk triboelectric nanogenerators in contact and non-contact modes *Nano Res.* **9** 1057–70
- [38] Niu S, Liu Y, Wang S, Lin L, Zhou Y S, Hu Y and Wang Z L 2014 Theoretical investigation and structural optimization of single-electrode triboelectric nanogenerators *Adv. Funct. Mater.* **24** 3332–40
- [39] Li Y, Cheng G, Lin Z H, Yang J, Lin L and Wang Z L 2015 Single-electrode-based rotary triboelectric nanogenerator and its applications as self-powered contact area and eccentric angle sensors *Nano Energy* **11** 323–32

- [40] Narasimulu A A *et al* 2017 Significant triboelectric enhancement using interfacial piezoelectric ZnO nanosheet layer *Nano Energy* **40** 471–80
- [41] Correa J C A J and Guzman A A L 2020 *Mechanical Vibrations and Conditional Monitoring* vol 7 (Amsterdam: Elsevier)
- [42] Mohammed Z, Elfadel I M (Abe) and Rasras M 2018 Monolithic multi degree of freedom (MDoF) capacitive MEMS accelerometers *Micromachines* **9** 1–20
- [43] Zhao S and Fu H 2018 A novel vibration sensor system for frequency measurement based on bias flip technique *Meas. J. Int. Meas. Confed.* **124** 56–63